Angewandte Chemie International Edition
www.angewandte.org

How to cite: *Angew. Chem. Int. Ed.* **2023,** *62,* e202300418
International Edition: doi.org/10.1002/anie.202300418
German Edition: doi.org/10.1002/ange.202300418

Zn–I$_2$ Batteries

A Janus Separator based on Cation Exchange Resin and Fe Nanoparticles-decorated Single-wall Carbon Nanotubes with Triply Synergistic Effects for High-areal Capacity Zn–I$_2$ Batteries

Yuanhong Kang, Guanhong Chen, Haiming Hua, Minghao Zhang, Jin Yang, Pengxiang Lin, Huiya Yang, Zeheng Lv, Qilong Wu, Jinbao Zhao, and Yang Yang**

Abstract: Zn–I$_2$ batteries stand out in the family of aqueous Zn-metal batteries (AZMBs) due to their low-cost and immanent safety. However, Zn dendrite growth, polyiodide shuttle effect and sluggish I$_2$ redox kinetics result in dramatically capacity decay of Zn–I$_2$ batteries. Herein, a Janus separator composed of functional layers on anode/cathode sides is designed to resolve these issues simultaneously. The cathode layer of Fe nanoparticles-decorated single-wall carbon nanotubes can effectively anchor polyiodide and catalyze the redox kinetics of iodine species, while the anode layer of cation exchange resin rich in –SO$_3^-$ groups is beneficial to attract Zn^{2+} ions and repel detrimental SO$_4^{2-}$/polyiodide, improving the stability of cathode/anode interfaces synergistically. Consequently, the Janus separator endows outstanding cycling stability of symmetrical cells and high-areal-capacity Zn–I$_2$ batteries with a lifespan over 2500 h and a high-areal capacity of 3.6 mAh cm^{-2}.

Introduction

Aqueous Zn metal batteries (AZMBs) have been studied extensively in the pursuit of low-cost, safe and long lifespan grid-scale electrochemical energy storage technology to meet the emerging demands for the utilization of renewable resources.[1–3] Differing from conventional AZMBs using transition metal oxides or Prussian blue analogues as the cathode, Zn–I$_2$ batteries have stood out due to the unique merits of I$_2$ cathode including wide abundance (50–60 μg L^{-1} of I$_2$ in seawater),[4] high theoretical capacity (211 mAh g^{-1}),[5] and immanent safety performance.[6] Despite the great superiorities, the advancement of the practical application of Zn–I$_2$ batteries is still facing some scientific challenges. In terms of the anode side, Zn dendrite formation and interface parasitic side reactions during cycling result in low Zn utilization and poor cycling stability.[7–12] For the I$_2$ cathode side, the poorly conductive I$_2$ will be electrochemically reduced to I$^-$ during the discharge process, which is inevitably accompanied by the generation of highly soluble polyiodide ($I_2+I^-\rightarrow I_3^-$, $I_2+I_3^-\rightarrow I_5^-$).[13] Polyiodide tends to dissolve from electrode to catholyte, resulting in the overcharge phenomenon and the consumption of active materials.[14] Moreover, the limited kinetics of bi-electron reaction of I$_2$ cathode exacerbate the loss of soluble polyiodide to the electrolyte by diffusion, resulting in poor rate performance.[15] More seriously, similar to polysulfide,[16–20] the polyiodide dissolved in the electrolyte undergo a shuttle effect, then diffuse to the Zn anode, further react with the Zn anode ($Zn+I_3^-\rightarrow Zn^{2+}+3I^-$), causing the uncontrollable self-discharge phenomenon and dramatically Zn corrosion.[21,22] The problems with Zn–I$_2$ batteries are complex and correlative, thus resolving them in both Zn anode and I$_2$ cathode simultaneously seems to be the ultimate route to realizing the successful commercialization of Zn–I$_2$ batteries.

To date, profuse strategies have been employed to address the above-mentioned problems. Against Zn metal anodes, constructing protective layers (e.g., MOFs,[23] ZnO,[24] nanoporous CaCO$_3$,[25] ZnS coatings[26]), optimizing electrolytes (e.g., electrolyte additives,[27–29] high-concentration electrolytes,[30] water-in-salt electrolytes[31]) and designing Zn-anode structures (e.g., building Zn metal alloy,[32] Zn anode etching[33]) have been reported, as approaches to effectively induce uniform deposition of Zn, restrain H$_2$ evolution and self-corrosion. Although these methods can improve the electrochemical reversibility of Zn metal anode in traditional AZMB systems, its interface stability surrounded by abundant I$_3^-$ and I$_5^-$ ions is questionable. On the other hand, to intercept polyiodide and address the problems of poor conductivity and low utilization for iodine, various explorations have been proposed for I$_2$ cathodes (e.g., starch,[34] porous carbon matrix,[35–38] quaternization engineering,[39] povidone,[40] double-layered cathodes[41]). The I$_2$ active species are usually anchored by physical/chemical adsorption or dense pores to prevent the escape/shuttle of polyiodide, whereas the above methods often fail to accelerate the redox kinetics of iodine species,[42,43] so that Zn–I$_2$ batteries exhibit unsatisfactory rate capability, and

---

[*] Y. Kang, G. Chen, H. Hua, M. Zhang, J. Yang, P. Lin, H. Yang, Z. Lv, Q. Wu, Prof. J. Zhao, Dr. Y. Yang
State Key Lab of Physical Chemistry of Solid Surfaces,
State-Province Joint Engineering Laboratory of Power Source Technology for New Energy Vehicle,
College of Chemistry and Chemical Engineering,
Xiamen University
Xiamen 361005 (China)
E-mail: jbzhao@xmu.edu.cn
yangyang419@xmu.edu.cn

the loading mass of I_2 active material in previous research is usually no exceeding $3\,mg\,cm^{-2}$, resulting in the relatively low energy density.

From a fundamental view, both anodic and cathodic reactions are closely associated with electrochemical interfaces, while the separator is an Indispensable component between the anode and cathode. Therefore, the modification of separators, does not involve the complex electrode design, seems to be a more direct and effective way to regulate the interfacial environment of both the anode and cathode.[44–49] Some pioneering investigations have verified that Zn^{2+} ion flux can be efficiently homogenized at the separator-anode interface by introducing functional constituents including $BaTiO_3$,[50] Mxene,[51,52] graphene[53,54] and sulfonic cellulose.[55] Moreover, some recent researches have been also proposed to alleviate the shuttle of polyiodide by constructing ion-sieving membranes (e.g., MOFs coatings,[56] zeolite molecular sieve membranes,[57] PEDOT: PSS,[58]). It should be noted that most of the separator modification approaches separately focus on either suppressing Zn dendrite growth or mitigating polyiodide shuttle effect. There are still few studies exhibiting simultaneous improvements in both anodic and cathodic performances in a whole $Zn–I_2$ battery system. Therefore, a proper design of the separator that can synergistically resolve the problems existing in the anode and cathode interfaces, meanwhile facilitating the reversible redox kinetics of iodine species is of considerable interest for the development of practical $Zn–I_2$ batteries.

Based on this inspiration, we exploited a multifunctional Janus separator for the synergistic regulation of anode/cathode interfaces, and reversible redox kinetics of iodine species for long-lifespan $Zn–I_2$ batteries. Such a Janus separator (Dowex + Fe-SCNT/GF) is composed of a commercial glass fiber (GF) separator with the cation exchange resin (Dowex) layer on the anode side and Fe metal nanoparticles-decorated single-wall carbon nanotubes (Fe-SCNT) layer on the cathode side, respectively. At the anode interface, the Dowex is a commercial cation exchange resin product of Dow Chemical Co. involving sulfonated cross-linked styrene-co-divinylbenzene. As illustrated in Figure 1a, abundant $–SO_3^-$ groups and generous channels inside Dowex microspheres effectively attract Zn^{2+} cations and exclude free SO_4^{2-} anions, which not only redistribute Zn^{2+}-flux but also reduce the desolvation energy barrier. The manipulated Zn anode interface chemistry is beneficial to the uniform Zn deposition behavior and the inhibition of side reactions and self-corrosion. Moreover, the highly negative-charge surface can also repel polyiodide due to the Coulomb effect to weaken the shuttle effect; At the cathode interface, the Fe-SCNT on the cathode side not only effectively physically adsorbs polyiodide and transports electrons by the SCNT with large specific surface area, but also chemically adsorbs and catalyzes polyiodide by Fe

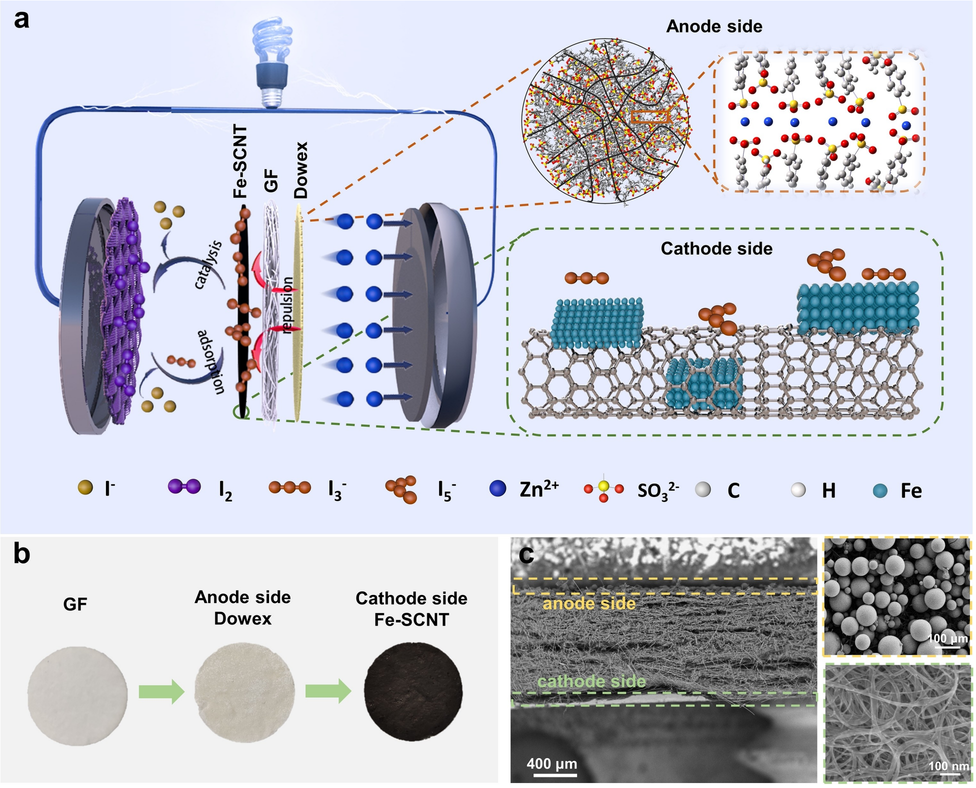

Figure 1. Mechanism illustration and basic characterization of Dowex + Fe-SCNT/GF separator. a) Mechanism diagram of Dowex + Fe-SCNT/GF separator. b) Optical images of Dowex + Fe-SCNT/GF separator. c) The scanning electron microscopy (SEM) images of Dowex + Fe-SCNT/GF separator section.

metal nanoparticles to promote the redox reaction kinetics of iodine species. The synchronous improvements of the adsorption effect and conversion kinetics efficiently prevent the diffusion of polyiodide to the anode, and further alleviate the corrosion of Zn metal. Considering the structural uniqueness and simplification of the manufacturing process, the proposed Janus separator design should provide promising opportunities for the development of high-areal capacity Zn–I_2 batteries with good application prospects.

Results and Discussion

From a fundamental view, the key to addressing the problems of Zn–I_2 batteries lies in manipulating the Zn^{2+} migration process on the anode side and anchoring the polyiodide on the cathode side synergistically. Although the proposed Dowex + Fe-SCNT/GF separator design is simple and facile, it can realize these collaborative functions specifically and pointedly. On the anode side of the Dowex + Fe-SCNT/GF separator, Dowex has a large amount of $-SO_3^-$ groups (the ion exchange capacity is measured to be 1.98 meq ml^{-1}, Figure S2), which are combined with Zn^{2+} through the ion exchange in Zn salt solution before using. It should be noted that the Zn^{2+} concentration storage in interconnected channels of Dowex microspheres is calculated to be 0.99 $mol\,L^{-1}$ after ion exchange, close to the bulk electrolyte concentration (1 M), which can redistribute Zn^{2+} ions at the interface and reduce the concentration polarization. Moreover, the negatively charged surface with $-SO_3^-$ groups on the anode side is also beneficial to repel the leaked polyiodide to prevent their contact with the Zn metal anode due to the electrostatic repulsion. On the cathode side of the Dowex + Fe-SCNT/GF separator, Fe-SCNT confines polyiodide to the cathode side of the separator by the synchronous chemisorption of Fe and physisorption of the C atoms, meanwhile, Fe metal nanoparticles also serve as the valid catalyst to accelerate redox chemistry of iodine. The Dowex + Fe-SCNT/GF separator is fabricated by a simple and scalable slurry coating method with different functional layers on both sides of the separator (Figure 1b). Since the Dowex is amorphous, three distinct diffusion peaks at 16.5°, 26.8° and 41.1° can be observed by X-ray diffraction (XRD) (Figure S3). As shown in Figure 1c, the Dowex layer on the anode side is composed of regular resin spheres ranging from 20–60 μm, and the relatively large specific surface area is in favor of carrying more $-SO_3^-$ groups. And the Fe-SCNT layer on the cathode side is composed of carbon nanotubes with diameters between 1–3 nm, and a large amount of Fe nanoparticles are uniformly distributed (Figure S4 and S5). Figure S6 shows that the additional coating layers show a negligible effect on the Zn^{2+} conductivity of the GF separator, which that of the Dowex/GF separator and GF separator maintains 14.60 $mS\,cm^{-1}$ and 10.39 $mS\,cm^{-1}$, respectively.

First, the effect of the Dowex coating layer on the Zn plating/stripping reversibility was investigated by assembling Zn||Cu half cells and Zn||Zn symmetrical cells by using a GF separator coated Dowex layers on both sides (denoted as Dowex/GF, Figure 2). Figure 2a shows that under the current density of 2 $mA\,cm^{-2}$ and the deposition capacity of 1 $mAh\,cm^{-2}$, the average coulombic efficiency of Zn||Cu half cells with the Dowex/GF separator maintained as high as 99.5 % after 1000 cycles. As a comparison, the coulombic efficiency begins to fluctuate dramatically after only 90 cycles with the GF separator, indicating the occurrence of an internal short circuit. Moreover, the polarization voltage with the Dowex/GF separator is more stable than that with the control GF separator, which is about 100 mV for the first cycle (Figure 2b and Figure S7). Subsequently, the Zn||Zn symmetrical cells with both separators were fabricated to further evaluate the cycling stability of Zn metal anodes. Figure 2c shows that the Zn||Zn symmetrical cell with the Dowex/GF separator exhibits an extraordinarily long lifespan of 2500 h under the conditions of 1 $mA\,cm^{-2}$ and 1 $mAh\,cm^{-2}$. However, the cycling stability of GF is obviously inferior, which shows a short circuit after 318 h. The cycling stability at the higher current densities of 5 and 10 $mA\,cm^{-2}$ for 1 $mAh\,cm^{-2}$ was also investigated (Figure S8 and S9). In addition, even under the higher current density/deposition capacity of 2 $mA\,cm^{-2}$/2 $mAh\,cm^{-2}$, the Zn||Zn symmetrical cell with the Dowex/GF separator still maintains an ultra-long cycle life of 2000 h (Figure S10), which is almost ten times that of the GF separator (only about 200 h). It is worth noting that the battery failure is closely associated with the solvation process at anode side: Zn^{2+} is combined with H_2O to form $[Zn(H_2O)_6]^{2+}$, which exists in the $ZnSO_4$ aqueous solution. Therefore, during the Zn deposition process, prior to the electron transfer between the substrate and Zn^{2+} ions at the interface, hydrated $[Zn(H_2O)_6]^{2+}$ must consume considerable energy to break free from the shackles of active H_2O, triggering the hydrogen evolution reaction (HER). The HER will cause the increase of local pH, resulting in the generation of $Zn_4SO_4(OH)_6\cdot 5H_2O$ by-products. Therefore, effectively reducing the desolvation energy is one of the most feasible routes to prolong the lifespan of Zn metal anode, which can be obtained by the Arrhenius equation from the electrochemical impedance spectroscopy (EIS) of Zn||Zn symmetrical cells at various temperatures. Figure S11 shows that the charge-transfer resistance with the Dowex/GF separator and GF separator gradually reduces with the increase of temperature. Figure 2d shows that Dowex layer can indeed reduce the desolvation energy of Zn^{2+}. The desolvation energy of GF is 44.5 $kJ\,mol^{-1}$, while the desolvation energy of Dowex/GF is only 26.7 $kJ\,mol^{-1}$. In addition, compared with GF (5.64 $mA\,cm^{-2}$), Dowex/GF shows a lower corrosion current (1.18 $mA\,cm^{-2}$), indicating that Dowex can effectively inhibit HER and Zn corrosion reaction (Figure S12). Moreover, Figure 2e–f demonstrates that the Dowex/GF separator also significantly increases the Zn^{2+} migration number ($t = 0.629$, Figure 2e), much higher than that of GF ($t = 0.417$, Figure 2f). Due to the preferred coordination between Zn^{2+} and $-SO_3^-$ groups of Dowex, the Dowex/GF separator endows a lower desolvation energy barrier, improved corrosion resistance, and higher Zn^{2+} migration number,

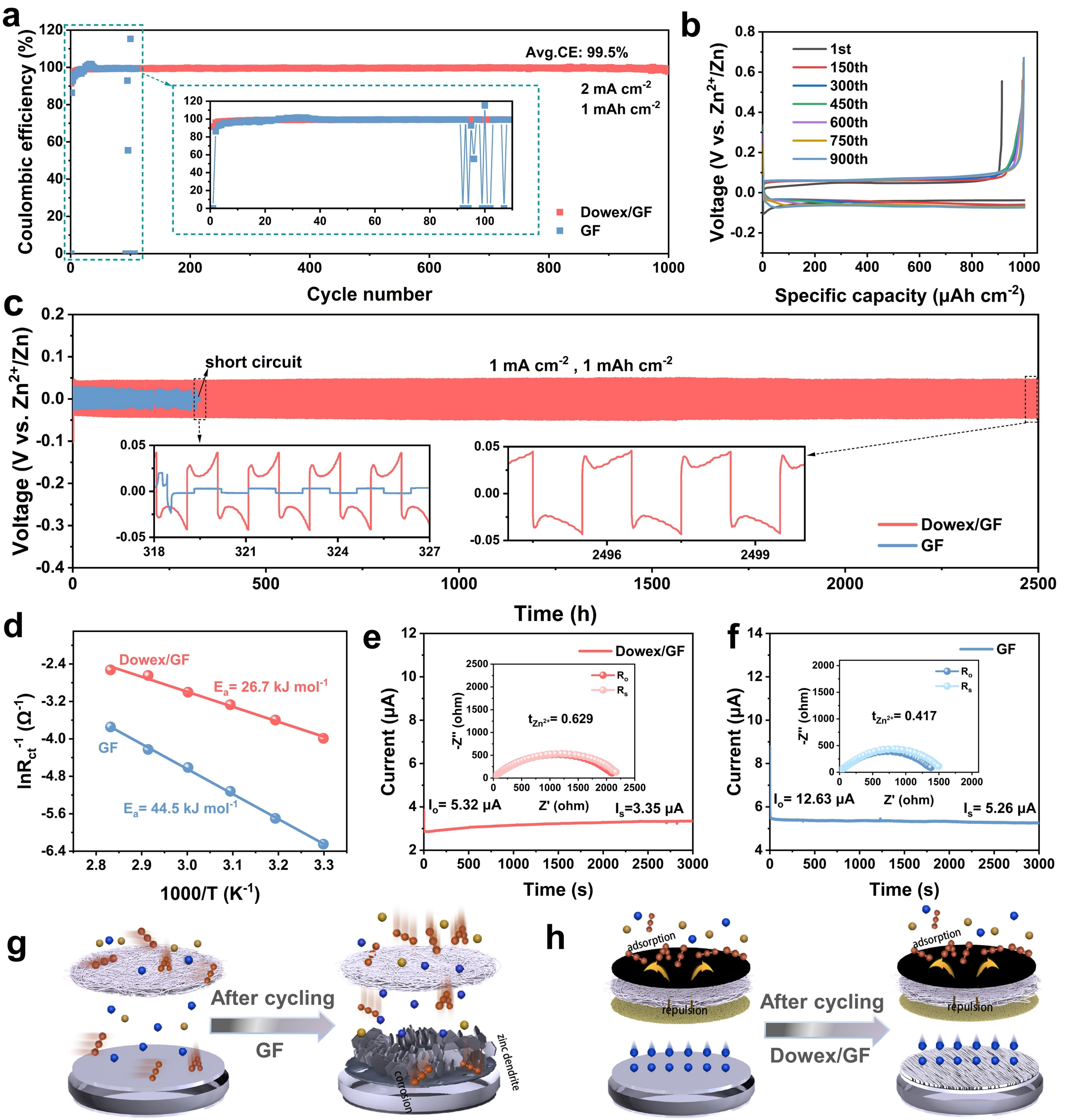

Figure 2. Characterization and mechanism research at Zn anode. a) The coulombic efficiency of the Zn||Cu cells with the GF separator and Dowex/GF separator, and b) the capacity-voltage profiles of the Zn||Cu cells with the Dowex/GF separator at 2 mA cm^{-2} and a Zn stripping capacity of 1 mAh cm^{-2}. c) The time-voltage profiles of the long-term cycling for the Zn||Zn cells with the GF separator and Dowex/GF separator at 1 mA cm^{-2} and 1 mAh cm^{-2}. d) The calculated desolvation activation energy with the GF separator and Dowex/GF separator by the Arrhenius equation. (e, f) Zn^{2+} transference number of e) the Dowex/GF separator, and f) GF separator at a polarization voltage of 10 mV for 3000 s. (g, h) Schematic illustration of the Zn^{2+} deposition process before/after cycling with g) the GF separator, and h) Dowex+Fe-SCNT/GF separator, respectively.

leading to highly reversible Zn deposition/stripping behavior (Figure 2g and 2 h).

In addition to the characterization of electrochemical performance, we also analyzed the Zn deposition morphology with both separators after 50 cycles (Figure 3a–e). SEM images show that the Zn anode surface with GF separator after cycling was covered with irregular Zn flakes (Figure 3a), while the Zn anode surface with Dowex/GF separator was rather uniform and compact (Figure 3d), and Zn dendrites were almost absent. The atomic force microscope (AFM) images further demonstrate that Dowex/GF separator contributes to the uniform deposition morphology

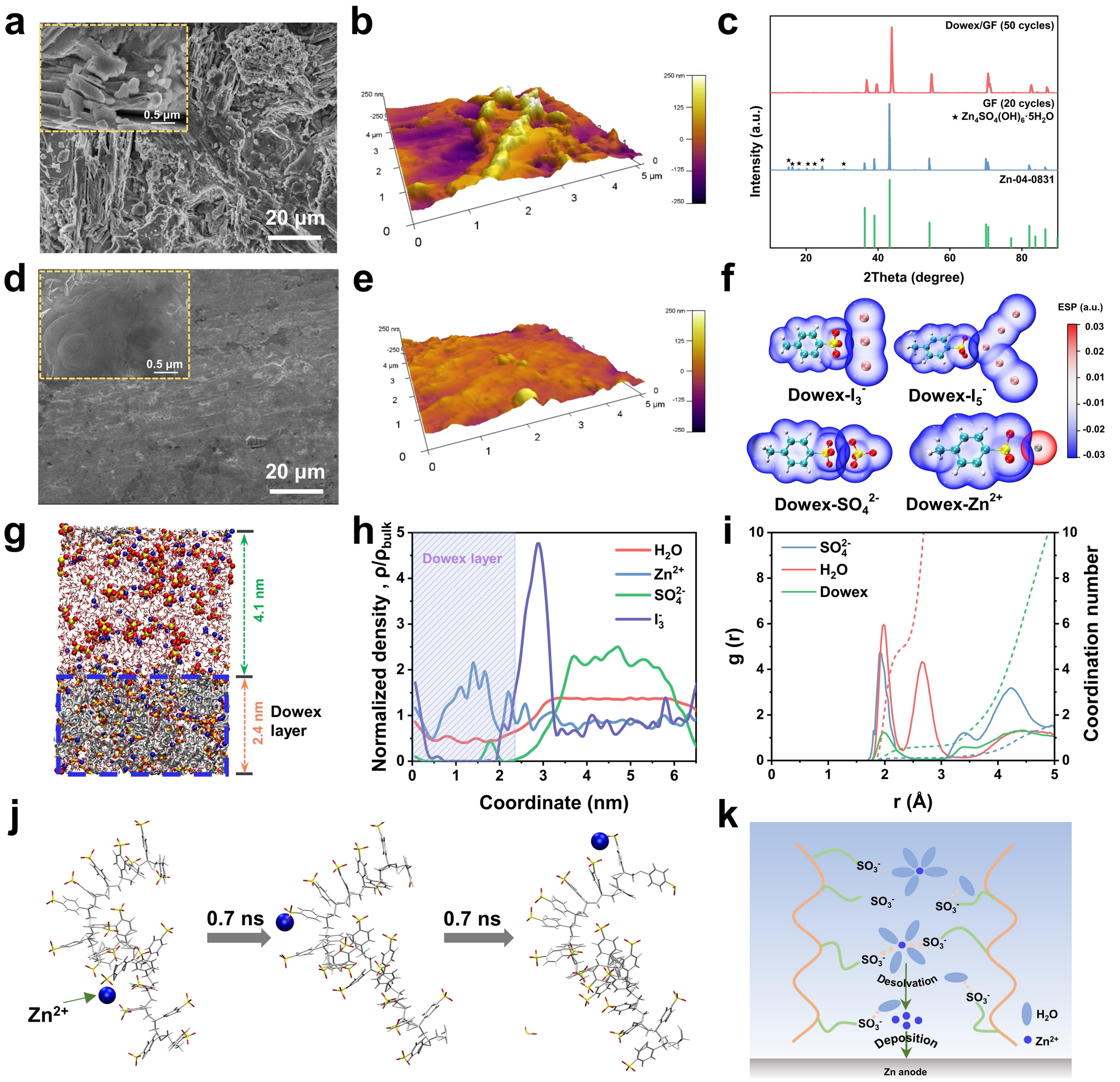

Figure 3. Deposition morphology and MD simulations of the Zn anode. a) SEM images, and b) AFM image of the Zn anode for Zn||Zn cells with GF separator after 50 cycles. c) XRD patterns of Zn anode for Zn||Zn cells with Dowex/GF separator and GF separator after cycling. d) SEM images, and e) AFM image of the Zn anode for Zn||Zn cells with Dowex/GF separator after 50 cycles. f) The electrostatic potential (ESP) images of the interaction between ions (I_3^-, I_5^-, SO_4^{2-} and Zn^{2+}) and the Dowex. g) The model of MD simulation for the Dowex-electrolyte interface. h) Normalized density profiles of the I_3^-, SO_4^{2-}, Zn^{2+} and H_2O in 1 M $ZnSO_4$ solution with Dowex layer. i) Coordination number profiles of the SO_4^{2-}, Dowex and H_2O around Zn^{2+} in 1 M $ZnSO_4$ solution with Dowex layer. j) Changes of the Zn^{2+} migration position along the polymer chain in Dowex with the passage of time. k) Schematic illustration of the Zn^{2+} desolvation and deposition process.

of Zn on the surface (Figure 3b, e and Figure S13). The composition of Zn anode surface after cycling was also examined by XRD. It was found that even after 50 cycles, the Zn anode with Dowex/GF separator basically remains the original state of Zn foil, without obvious by-products detected. In sharp contrast, the $Zn_4SO_4(OH)_6$·$5H_2O$ by-products appear in the Zn anode with GF only after 20 cycles, which further verifies that Dowex coating layer could inhibit the side reaction. Besides, the density functional theory (DFT) calculations and molecular dynamics (MD) simulations were carried out to deeply understand the inherent modification mechanism of the Dowex layer (Figure 3f–j). Figure 3f shows that $-SO_3^-$ is negatively charged and mutually repels I_3^-, I_5^- and SO_4^{2-} with a similarly negative charge, and it is easy to adsorb with positively charged Zn^{2+}, which is beneficial to the Zn^{2+} transport and desolvation process. In order to simulate the interaction between ions/H_2O and the Dowex layer in the real electrolyte, MD simulation is conducted and the constructed model is shown in Figure 3g. Figure 3h shows that the Dowex layer contains more Zn^{2+} cations, yet less H_2O, while I_3^- and SO_4^{2-} anions are almost all distributed in the $ZnSO_4$ solution, which is consistent with Figure 3f. These results confirm the repulsion of polyiodide or SO_4^{2-} and the adsorption of Zn^{2+} for Dowex layer. Thus, the mobility of Zn^{2+} is accelerated, and the decrease of active H_2O in the Dowex layer may constrain the appearance of HER by reducing the corresponding reactant near the reaction interface. The simulated solvation structure of bulk 1 M $ZnSO_4$ aqueous electrolyte is about $Zn^{2+}(H_2O)_6$ (Figure S14), which is in agreement with previous research. However, $–SO_3^-$ groups of Dowex tend to interact with Zn^{2+} to replace partial H_2O molecules in the solvated sheath, leading to the regulated solvation structure of $–SO_3^-–Zn^{2+}(H_2O)_5$ (Figure 3i), which should be beneficial to the movement of H_2O molecules during the desolvation process. Meanwhile, $–SO_3^-$ groups in the polymer chains also serve as active sites for the transport of Zn^{2+} ions, which is verified by the snapshots of a single Zn^{2+} at different times (Figure 3j). Therefore, the abundant channels formed by polymer chains in Dowex efficiently homogenize the Zn^{2+} ion flux, and finally make it uniformly deposited on the surface of the Zn anode. Figure 3k further illustrates how $–SO_3^-$ can reduce Zn^{2+} desolvation and achieve uniform deposition. Consequently, the DFT calculation and MD simulation well explain the derivation of desolvation regulation and homogenization of Zn^{2+} flux in Dowex from another perspective, which is in perfect agreement with the previous experimental results.

Focusing on the I_2 cathode side, we tried to get deep insight into the mechanism that the cathode side coating of Dowex+Fe-SCNT/GF can effectively inhibit the shuttle effect of polyiodide (I_3^-, I_5^-) and electrocatalysis redox kinetics of iodine. Therefore, pure SCNT without Fe nanoparticles was also prepared by the acid treatment, which is used to construct the Dowex+SCNT/GF separator for comparison. Firstly, an H-type glass cell was used to visualize the polyiodide diffusion experiment: the left chamber was filled with brown-yellow 1 M I_3^- solution, and the right chamber was filled with transparent 1 M $ZnSO_4$ solution. After the duration of 60 mins, the color of the GF-based H-type cell became the darkest, followed by Dowex+SCNT/GF, while the color of the Dowex+Fe-SCNT/GF-based H-type cell was almost unchanged. (Figure 4a and Figure S15). Meanwhile, the concentration of I^- and I_3^- ions in the right chamber was qualitatively studied by the in situ ultraviolet-visible spectroscopy (UV/Vis) measurement, and the concentration of I_3^- was calculated from the standard curve (Figure S16). It can be explicitly seen that a large amount of I^- and I_3^- anions pass through the GF separator in between through the concentration diffusion (Figure 4b), that the concentration of I_3^- reaches 0.646 M after 100 mins. For the Dowex+SCNT/GF without Fe nanoparticles (Figure S17), the diffusion of I_3^- anions is impeded to a certain degree, which is reduced to 0.186 M after 120 mins. Whereas the barrier effect toward I^- is negligible. For the Dowex+Fe-SCNT/GF separator, the penetrative I^- concentration is significantly reduced and no peak signal of I_3^- anions is detected. Combing these above results, it can be deduced that the physical adsorption of SCNT and charge repulsion of $–SO_3^-$ groups in Dowex may be not sufficiently effective to block the shuttle of polyiodide ions, particularly under high-loading mass conditions. Nonetheless, with the assistance of the chemical adsorption effect of Fe nanoparticles, the synergistic effect of the three components makes Dowex +Fe-SCNT/GF effectively confine polyiodide ions on the cathode side of the separator. In addition to the inhibition of polyiodide, the fast redox kinetics of I_2/I^- is also necessary for the stable cycling of I_2 cathode, which is expected to be realized by highly active reaction sites of Fe nanoparticles. The transmission electron microscopy (TEM) images verify that there is a large amount of Fe nanoparticles loaded on Fe-SCNT (Figure 4d), while Fe metal can hardly be seen in SCNT (Figure 4e). The Fe content quantitatively determined by inductively coupled plasma (ICP) method was 14.28 % in Fe-SCNT, while that was only 0.32 % in SCNT (Figure S18). Next, SCNT and Fe-SCNT were made into inks, then loaded on the glassy carbon electrodes to investigate their redox catalysis for I_2/I^- through cyclic voltammetry (CV) curves. The redox peaks in the CV curves are attributed to the transition of I_2/I^- (Figure 4f). It can be seen that Fe-SCNT has a higher peak current and a smaller polarization potential than SCNT. According to the Tafel curve (Figure 4g), it is found that, compared with SCNT (92.65 $mV\,dec^{-1}$), Fe-SCNT has a smaller slope (51.06 $mV\,dec^{-1}$), which indicates that Fe-SCNT can accelerate the redox kinetics of I_2/I^-. In order to testify whether Fe-SCNT can integrally play the role of adsorption and catalysis in the real battery system, we performed in situ Raman characterization (Figure 4h, 4i and Figure S19, S20). It can be seen that during the constant current charge–discharge process, GF has the strongest peaks of the I^- and polyiodide (Figure S20), and the peak intensity of Dowex+SCNT/GF is relatively weakened (Figure 4i), while Dowex+Fe-SCNT/GF almost does not appear obvious peaks of I^- and polyiodide during the discharge process (Figure 4h). In addition, the adsorption and catalytic mechanism of Fe-SCNT were studied in depth by DFT calculation. That the polyiodide adsorbed on the inside and outside of SCNT and the surface of Fe metal was calculated, respectively, and then the charge differential density diagram was obtained (Figure 4j, 4k and Figure S21–23). It can be obviously seen that the electron cloud of polyiodide flows to SCNT and especially Fe metal. As a result, the configuration of I_3^- and I_5^- changes, the length of the I–I bond becomes longer and the length of Fe–I bond is shortened, indicating that I^- is preferred to be formed. Figure 4l shows that Fe metal has stronger adsorption energies (−7.08 eV, −12.51 eV) with I_3^- and I_5^-, respectively. Above all, it can be speculated that polyiodide are prone to be chemically adsorbed on the Fe metal and the I–I bonds in polyiodide are broken to generate I^-, thus the redox kinetic of I_2/I^- is catalyzed and accelerated, meanwhile the electrolyte contains more I^-, which is conducive to the oxidation of I^- to I_2.

To date, since the mass of I_2 loaded on the carbon matrix does not exceed 3 $mg\,cm^{-2}$ in most of previously reported static Zn–I_2 batteries, the areal specific capacity of Zn–I_2 batteries is usually lower than 0.6 $mAh\,cm^{-2}$, which fails to

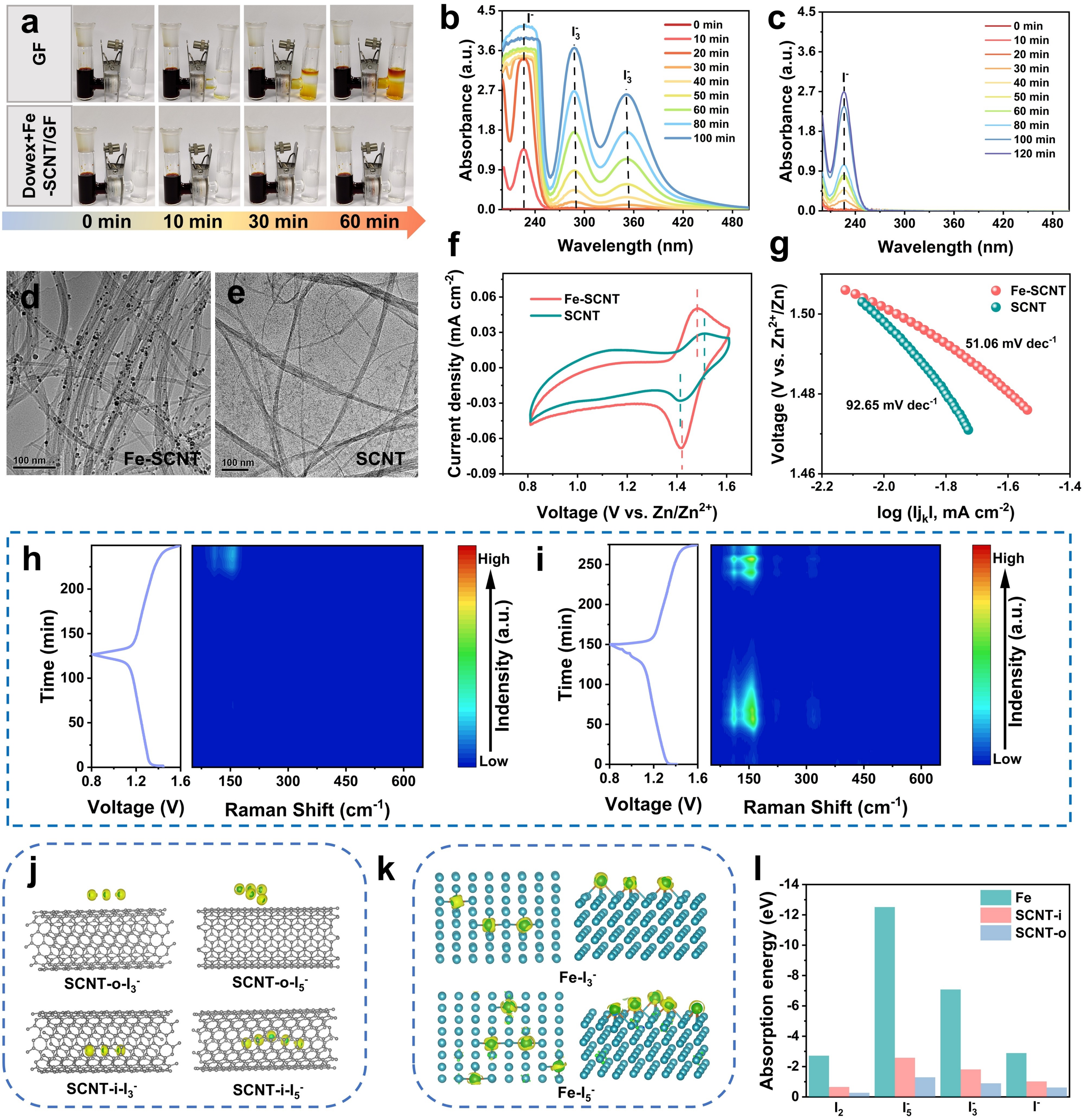

Figure 4. Inhibiting shuttle effect of polyiodide and accelerating redox at I_2 cathode. a) Optical images of visual shuttle effect by H-type glass cells with the I_3^- solution (1 M KI and 0.1 M I_2) for GF separator and Dowex+Fe-SCNT/GF separator. (b, c) UV/Vis curves of 1 M $ZnSO_4$ in the right chamber of H-type cell to determine the concentration of the I^- and I_3^- with b) GF separator, and c) Dowex+Fe-SCNT/GF separator. (d, e) TEM images of the single-wall carbon nanotubes loaded d) with Fe metal (Fe-SCNT), and e) without Fe metal (SCNT). f) CV curves of the Fe-SCNT and SCNT electrocatalysts in nitrogen saturated 1 M $ZnSO_4$ + 5 mM I_2 solution using three-electrodes electrolytic cells. g) Corresponding Tafel plots from CV curves. (h, i) In situ Raman spectrum of the I^- and I_3^- during the constant current charge–discharge process with h) the Dowex+Fe-SCNT/GF separator, and i) the Dowex+SCNT/GF separator. (j, k) The charge differential density of that I_3^-, I_5^- j) adsorbed inside and outside of SCNT, and k) adsorbed on the surface of Fe metal, respectively (green and yellow color indicate charge depletion and accumulation, respectively). l) The energies of that I_2, I^-, I_3^-, I_5^- adsorbed inside and outside of SCNT, and adsorbed on the surface of Fe metal, respectively.

meet the requirements of practical applications. Therefore, in order to evaluate the superiority of the Dowex+Fe-SCNT/GF separator in high areal capacity Zn–I_2 batteries, the mass of the I_2 active material loaded on the carbon cloth is controlled to be as high as 8–9 mg cm^{-2} with 1 M $ZnSO_4$ electrolyte. The capacity contribution of Fe-SCNT and carbon cloth is negligible for high areal capacity Zn–I_2 batteries (Figure S24 and S25). Figure S26 confirms that the Dowex and Fe-SCNT can improve the stability of cathode/anode interfaces synergistically. As shown in Figure 5a, the

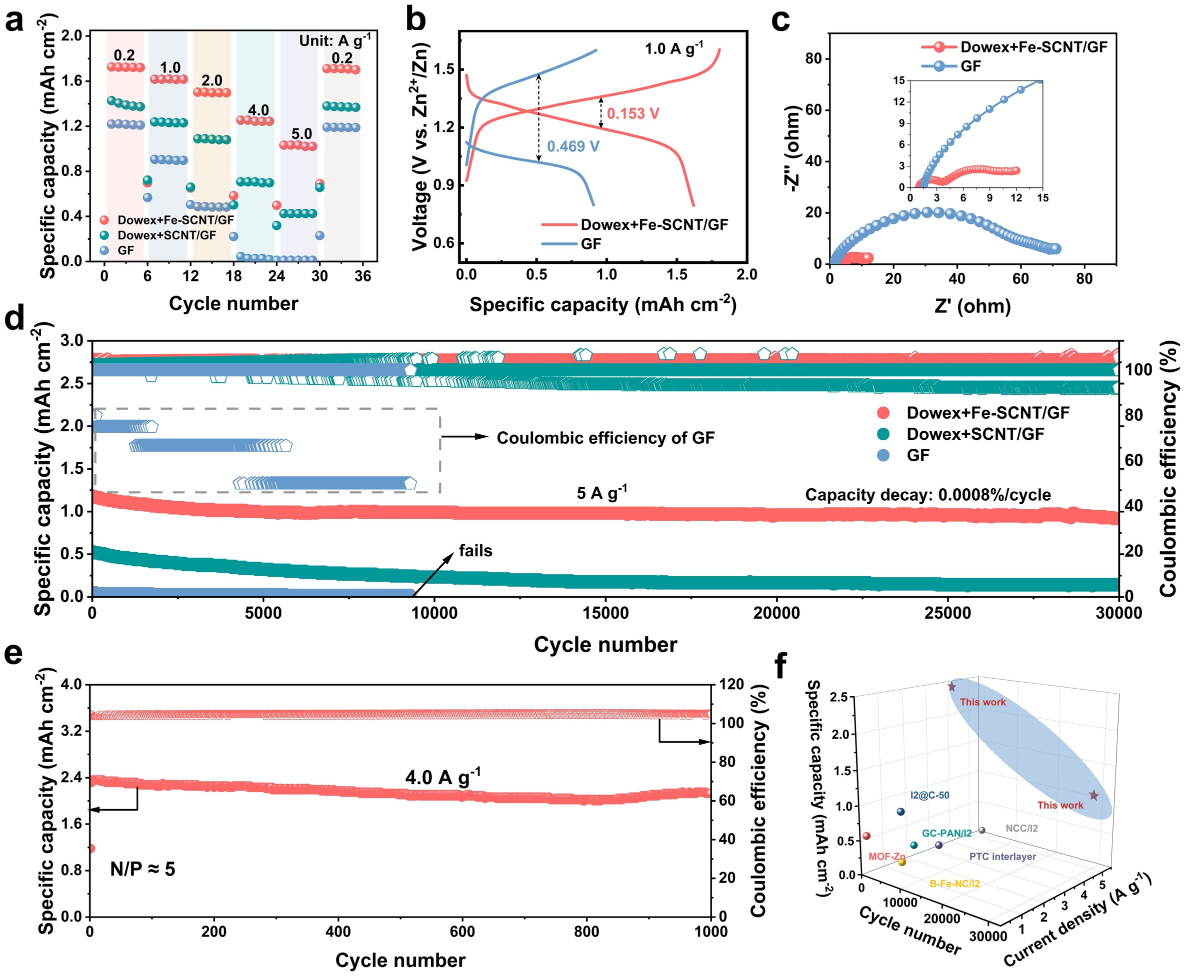

Figure 5. Ultra-stable aqueous high-areal capacity Zn–I_2 batteries. a) Rate performances for the Zn–I_2 batteries with GF separator, Dowex + SCNT/GF separator and Dowex + Fe-SCNT/GF separator at the current densities of 0.2, 1.0, 2.0, 4.0, 5.0 and 0.2 A g^{-1}. b) Galvanostatic charge/discharge curves of Zn–I_2 batteries with GF separator and Dowex + Fe-SCNT/GF separator at 1.0 A g^{-1}. c) The EIS of Zn–I_2 batteries with GF separator and Dowex + Fe-SCNT/GF separator after cycling. d) The long-cycling performance of Zn–I_2 batteries with GF separator, Dowex + SCNT/GF separator and Dowex + Fe-SCNT/GF separator at a current density of 5.0 A g^{-1}. e) Cycling performance of Zn–I_2 batteries at N/P ≈ 5 with the I_2 loading mass of ~20 mg cm^{-2}, for Dowex + Fe-SCNT/GF separator at a current density of 4.0 A g^{-1}. f) The battery performance comparison with reported Zn–I_2 batteries that I_2 was loaded on the carbon matrix.

Zn–I_2 batteries with Dowex + Fe-SCNT/GF separator shows a better rate performance than with GF separator. It delivers areal specific capacities of 1.72, 1.62, 1.50, 1.25, 1.03 mAh cm^{-2} at the current densities of 0.2, 1.0, 2.0, 4.0, 5.0 A g^{-1}, respectively. When the current density turns back to 0.2 A g^{-1}, the areal specific capacity can still recover to 1.71 mAh cm^{-2}, exhibiting excellent rate stability. Figure 5b shows that the polarization voltage of the Zn–I_2 battery with the Dowex + Fe-SCNT/GF separator (0.153 V) is substantially smaller than that of GF separator (0.469 V) at 1.0 A g^{-1}, corroborating the aforementioned Fe-SCNT that can accelerate the redox kinetics of iodine species. Furthermore, compared to the Zn–I_2 battery with GF separator (59.79 Ω), the impedance of that with Dowex + Fe-SCNT/GF separator is only 10.4 Ω after cycling, confirming that Fe-SCNT immensely reduces the charge transfer resistance. Incredibly, (Figure 5d) at a high current density of 5 A g^{-1}, the Zn–I_2 battery with Dowex + Fe-SCNT/GF separator still maintains an average capacity decay rate of only 0.0008 %/cycle after more than 30000 cycles, showing a stable coulombic efficiency close to 100 %. However, the Zn–I_2 battery with GF separator delivers no capacity, and the specific capacity of Dowex + SCNT/GF separator is also significantly lower. As a result, it is more beneficial for Dowex + Fe-SCNT/GF separator to exert adsorption and catalysis and accelerate the reaction kinetics at higher rates. Moreover, Figure S27 also reveals the effective inhibition of polyiodide shuttle effect even at a relatively low current density of 0.4 A g^{-1}. To further enhance the Zn utilization, the Zn–I_2 full batteries with a thin Zn foil (40 μm and 30 μm) as the anode and the ultra-high loading mass of I_2 to ~20 mg cm^{-2} as the cathode were also fabricated. As shown in Figure S28, the areal capacity of such a Zn–I_2 full battery reaches a record-breaking value of ~3.6 mAh cm^{-2} at a current density of 0.2 A g^{-1}, and the N/P ratio is determined to be only ~5. At a high current density of 4 A g^{-1} (the areal current density reaches an extremely high value of $85\ \mathrm{mA\,cm^{-2}}$ at the anode side), the Zn–I_2 full battery with the Dowex + Fe-SCNT/GF separator can still cycle stably for more than 1000 cycles, with a reversible areal capacity as high as $2.4\ \mathrm{mAh\,cm^{-2}}$ (Figure 5e and Figure S30). Moreover, at a slightly lower current density of $2\ \mathrm{A\,g^{-1}}$, the specific capacity reaches a new high level of $2.8\ \mathrm{mAh\,cm^{-2}}$ with excellent cycling stability (Figure S29 and S31). Compared with the previously reported literature about Zn–I_2 batteries (Table S1), the Zn–I_2 battery with Dowex + Fe-SCNT/GF separator is prominent while considering the evaluation indexes of areal capacity, cycle number and rate capability comprehensively (Figure 5f).

Conclusion

In summary, aiming at parasitic reactions of Zn^{2+}, the shuttling effect of polyiodide and sluggish redox kinetics of iodine species, a multifunctional Janus separator is exploited. The Dowex layer and Fe-SCNT layer are introduced on the anode/cathode sides of commercial GF separators, respectively, by a simple and scalable slurry coating method. The SCNT physically adsorbs polyiodide and Fe nanoparticles chemically adsorb and catalyze iodine species for the Fe-SCNT coating, meanwhile, the Dowex coating can repel SO_4^{2-}/polyiodide and coordinates Zn^{2+} to reduce the desolvation energy and homogenize the flow of Zn^{2+}, which are proved by various experimental characterizations and theoretical calculations. Consequently, the Zn||Zn symmetrical cell with the modified separator retains stable cycling over 2500 h at $1\ \mathrm{mA\,cm^{-2}}/1\ \mathrm{mAh\,cm^{-2}}$. For Zn–$I_2$ full batteries, the Dowex + Fe-SCNT/GF separator exhibits outstanding cycling stability with an average capacity decay of 0.0008 %/cycle at $5\ \mathrm{A\,g^{-1}}$ after more than 30000 cycles, while GF separator has almost no capacity. Further controlling the N/P ratio to be ~5 and the ultra-high I_2 mass of $\sim 20\ \mathrm{mg\,cm^{-2}}$, it can still cycle stably for more than 1000 cycles with the high areal specific capacity of $2.4\ \mathrm{mAh\,cm^{-2}}$ at $4\ \mathrm{A\,g^{-1}}$. In view of the structural uniqueness and simplification of the manufacturing process, the designed Janus separator should provide a promising route for the commercial application of high-areal capacity Zn–I_2 batteries.

Acknowledgements

The authors gratefully acknowledge the financial support from National Natural Science Foundation of China (No. 22109030 and 22021001), Fundamental Research Funds for the Central Universities (20720220073), Fujian Industrial Technology Development and Application Plan (2022I0002), The Key Research and Development Program of Yunnan Province (202103AA080019) and Guangdong Basic and Applied Basic Research Foundation (No. 2021A1515010177), Beijng PARATERA Tech CO. Ltd. for providing HPC resources that have contributed to the research results reported within this paper. URL: https://paratera.com/

Conflict of Interest

The authors declare no conflict of interest.

Data Availability Statement

The data that support the findings of this study are available from the corresponding author upon reasonable request.

Keywords: Cation Exchange Resin · Fe Nanoparticles-Decorated Single-Wall Carbon Nanotube · Janus Separator · Redox Kinetics · Zinc-Iodine Batteries

[1] Y. Yang, C. Liu, Z. Lv, H. Yang, Y. Zhang, M. Ye, L. Chen, J. Zhao, C. C. Li, *Adv. Mater.* **2021**, *33*, 2007388.
[2] C. P. Grey, J. M. Tarascon, *Nat. Mater.* **2017**, *16*, 45–56.
[3] X. Qu, Y. Tang, X. He, J. Zhou, Z. Tang, W. Feng, J. Liu, *J. Electrochem. Soc.* **2022**, https://doi.org/10.13208/j.electrochem.211026.
[4] J. Ma, M. Liu, Y. He, J. Zhang, *Angew. Chem. Int. Ed.* **2021**, *60*, 12636–12647.
[5] J. Ma, M. Wang, H. Zhang, L. Fu, W. Zhang, B. Song, S. Lu, Q. Chen, K. Lu, *Mater. Today Energy* **2022**, *30*, 101146.
[6] D. Lin, Y. Li, *Adv. Mater.* **2022**, *34*, 2108856.
[7] D. J. Arnot, M. B. Lim, N. S. Bell, N. B. Schorr, R. C. Hill, A. Meyer, Y. Cheng, T. N. Lambert, *Adv. Energy Mater.* **2021**, *11*, 2101594.
[8] Q. Zhang, J. Luan, Y. Tang, X. Ji, H. Wang, *Angew. Chem. Int. Ed.* **2020**, *59*, 13280–13291.
[9] L. Hong, X. Wu, L. Y. Wang, M. Zhong, P. Zhang, L. Jiang, W. Huang, Y. Wang, K. X. Wang, J. S. Chen, *ACS Nano* **2022**, *16*, 6906–6915.
[10] A. Naveed, H. Yang, J. Yang, Y. Nuli, J. Wang, *Angew. Chem. Int. Ed.* **2019**, *58*, 2760–2764.
[11] Q. Jian, Y. Wan, Y. Lin, M. Ni, M. Wu, T. Zhao, *ACS Appl. Mater. Interfaces* **2021**, *13*, 52659–52669.
[12] L. Zhang, J. Huang, H. Guo, L. Ge, Z. Tian, M. Zhang, J. Wang, G. He, T. Liu, J. Hofkens, D. J. L. Brett, F. Lai, *Adv. Energy Mater.* **2023**, https://doi.org/10.1002/aenm.202203790.
[13] C. Chen, Z. Li, Y. Xu, Y. An, L. Wu, Y. Sun, H. Liao, K. Zheng, X. Zhang, *ACS Sustainable Chem. Eng.* **2021**, *9*, 13268–13276.
[14] J. Yang, Y. Song, Q. Liu, A. Tang, *J. Mater. Chem. A* **2021**, *9*, 16093–16098.
[15] Z. Pei, Z. Zhu, D. Sun, J. Cai, A. Mosallanezhad, M. Chen, G. Wang, *Mater. Res. Bull.* **2021**, *141*, 111347.
[16] J. Xu, H. Zhang, F. Yu, Y. Cao, M. Liao, X. Dong, Y. Wang, *Angew. Chem. Int. Ed.* **2022**, *61*, e202211933.
[17] X. Liu, J. Huang, Q. Zhang, L. Mai, *Adv. Mater.* **2017**, *29*, 1601759.
[18] C. Song, Z. Li, L. Ma, M. Li, S. Huang, X. Hong, Y. Cai, Y. Lan, *ACS Nano* **2021**, *15*, 13436–13443.
[19] D. Zhou, X. Tang, X. Guo, P. Li, D. Shanmukaraj, H. Liu, X. Gao, Y. Wang, T. Rojo, M. Armand, G. Wang, *Angew. Chem. Int. Ed.* **2020**, *59*, 16725–16734.
[20] Y. Li, T. Gao, D. Ni, Y. Zhou, M. Yousaf, Z. Guo, J. Zhou, P. Zhou, Q. Wang, S. Guo, *Adv. Mater.* **2022**, *34*, 2107638.
[21] S. Liu, W. Shang, Y. Yang, D. Kang, C. Li, B. Sun, L. Kang, S. Yun, F. Jiang, *Batteries Supercaps* **2022**, *5*, e202100221.
[22] C. Xie, H. Zhang, W. Xu, W. Wang, X. Li, *Angew. Chem. Int. Ed.* **2018**, *57*, 11171–11176.
[23] Z. Huang, W. Zhang, H. Zhang, L. Fu, B. Song, W. Zhang, Q. Chen, K. Lu, *J. Power Sources* **2022**, *523*, 231036.

[24] J. Y. Kim, G. Liu, G. Y. Shim, H. Kim, J. K. Lee, *Adv. Funct. Mater.* **2020**, *30*, 2004210.

[25] L. Kang, M. Cui, F. Jiang, Y. Gao, H. Luo, J. Liu, W. Liang, C. Zhi, *Adv. Energy Mater.* **2018**, *8*, 1801090.

[26] J. Hao, B. Li, X. Li, X. Zeng, S. Zhang, F. Yang, S. Liu, D. Li, C. Wu, Z. Guo, *Adv. Mater.* **2020**, *32*, 2003021.

[27] J. Cao, D. Zhang, X. Zhang, Z. Zeng, J. Qin, Y. Huang, *Energy Environ. Sci.* **2022**, *15*, 499–528.

[28] Z. Hu, F. Zhang, Y. Zhao, H. Wang, Y. Huang, F. Wu, R. Chen, L. Li, *Adv. Mater.* **2022**, *34*, 2203104.

[29] C. Li, A. Shyamsunder, A. G. Hoane, D. M. Long, C. Y. Kwok, P. G. Kotula, K. R. Zavadil, A. A. Gewirth, L. F. Nazar, *Joule* **2022**, *6*, 1103–1120.

[30] Y. Zhu, J. Yin, X. Zheng, A. H. Emwas, Y. Lei, O. F. Mohammed, Y. Cui, H. N. Alshareef, *Energy Environ. Sci.* **2021**, *14*, 4463–4473.

[31] Y. Zhang, G. Wan, N. H. C. Lewis, J. Mars, S. E. Bone, H. Steinrück, M. R. Lukatskaya, N. J. Weadock, M. Bajdich, O. Borodin, A. Tokmakoff, M. F. Toney, E. J. Maginn, *ACS Energy Lett.* **2021**, *6*, 3458–3463.

[32] M. Kwon, J. Lee, S. Ko, G. Lim, S. H. Yu, J. Hong, M. Lee, *Energy Environ. Sci.* **2022**, *15*, 2889–2899.

[33] J. Zheng, Y. Deng, J. Yin, T. Tang, R. Garcia-Mendez, Q. Zhao, L. A. Archer, *Adv. Mater.* **2022**, *34*, 2106867.

[34] S. Zhang, J. Hao, H. Li, P. Zhang, Z. Yin, Y. Li, B. Zhang, Z. Lin, S. Qiao, *Adv. Mater.* **2022**, *34*, 2201716.

[35] J. Xu, J. Wang, L. Ge, J. Sun, W. Ma, M. Ren, X. Cai, W. Liu, J. Yao, *J. Colloid Interface Sci.* **2022**, *610*, 98–105.

[36] H. Pan, B. Li, D. Mei, Z. Nie, Y. Shao, G. Li, X. S. Li, K. S. Han, K. T. Mueller, V. Sprenkle, J. Liu, *ACS Energy Lett.* **2017**, *2*, 2674–2680.

[37] Y. Hou, F. Kong, Z. Wang, M. Ren, C. Qiao, W. Liu, J. Yao, C. Zhang, H. Zhao, *J. Colloid Interface Sci.* **2022**, *629*, 279–287.

[38] Q. Guo, H. Wang, X. Sun, Y. Yang, N. Chen, L. Qu, *ACS Mater. Lett.* **2022**, *4*, 1872–1881.

[39] L. Zhang, M. Zhang, H. Guo, Z. Tian, L. Ge, G. He, J. Huang, J. Wang, T. Liu, I. P. Parkin, F. Lai, *Adv. Sci.* **2022**, *9*, 2105598.

[40] Y. Zhang, D. Tao, F. Xu, T. Li, *Chem. Eng. J.* **2022**, *427*, 131592.

[41] D. Lin, D. Rao, S. Chiovoloni, S. Wang, J. Q. Lu, Y. Li, *Nano Lett.* **2021**, *21*, 4129–4135.

[42] M. Liu, Q. Chen, X. Cao, D. Tan, J. Ma, J. Zhang, *J. Am. Chem. Soc.* **2022**, *144*, 21683–21691.

[43] T. Liu, H. Wang, C. Lei, Y. Mao, H. Wang, X. He, X. Liang, *Energy Storage Mater.* **2022**, *53*, 544–551.

[44] J. Liang, Q. Chen, X. Liao, P. Yao, B. Zhu, G. Lv, X. Wang, X. Chen, J. Zhu, *Angew. Chem. Int. Ed.* **2020**, *59*, 6561–6566.

[45] F. Ilyas, J. Chen, Y. Zhang, H. Lu, Y. Huang, H. Ma, J. Wang, *Angew. Chem. Int. Ed.* **2022**, *61*, e202215110.

[46] Y. Liu, X. Lu, F. Lai, T. Liu, P. R. Shearing, I. P. Parkin, G. He, D. J. L. Brett, *Joule* **2021**, *5*, 2845–2903.

[47] H. Dong, J. Li, J. Guo, F. Lai, F. Zhao, Y. Jiao, D. J. L. Brett, T. Liu, G. He, I. P. Parkin, *Adv. Mater.* **2021**, *33*, 2007548.

[48] W. Zong, H. Guo, Y. Ouyang, L. Mo, C. Zhou, G. Chao, J. Hofkens, Y. Xu, W. Wang, Y. Miao, G. He, I. P. Parkin, F. Lai, T. Liu, *Adv. Funct. Mater.* **2022**, *32*, 2110016.

[49] M. S. Gonzalez, Q. Yan, J. Holoubek, Z. Wu, H. Zhou, N. Patterson, V. Petrova, H. Liu, P. Liu, *Adv. Mater.* **2020**, *32*, 1906836.

[50] Y. Liang, D. Ma, N. Zhao, Y. Wang, M. Yang, J. Ruan, G. Yang, H. Mi, C. He, P. Zhang, *Adv. Funct. Mater.* **2022**, *32*, 2112936.

[51] Y. Su, B. Liu, Q. Zhang, J. Peng, C. Wei, S. Li, W. Li, Z. Xue, X. Yang, J. Sun, *Adv. Funct. Mater.* **2022**, *32*, 2204306.

[52] W. Yang, Q. Han, W. Li, M. Wu, J. Yao, M. Zhao, X. Lu, *Energy Storage Mater.* **2022**, *52*, 29–39.

[53] C. Li, Z. Sun, T. Yang, L. Yu, N. Wei, Z. Tian, J. Cai, J. Lv, Y. Shao, M. H. Rümmeli, J. Sun, Z. Liu, *Adv. Mater.* **2020**, *32*, 2003425.

[54] J. Cao, D. Zhang, C. Gu, X. Wang, S. Wang, X. Zhang, J. Qin, Z. Wu, *Adv. Energy Mater.* **2021**, *11*, 2101299.

[55] X. Zhang, J. Li, K. Qi, Y. Yang, D. Liu, T. Wang, S. Liang, B. Lu, Y. Zhu, J. Zhou, *Adv. Mater.* **2022**, *34*, 2205175.

[56] H. Yang, Y. Qiao, Z. Chang, H. Deng, P. He, H. Zhou, *Adv. Mater.* **2020**, *32*, 2004240.

[57] Z. Li, X. Wu, X. Yu, S. Zhou, Y. Qiao, H. Zhou, S. Sun, *Nano Lett.* **2022**, *22*, 2538–2546.

[58] Y. Zhang, T. Zhao, S. Yang, Y. Zhang, Y. Ma, Z. Wang, *J. Energy Chem.* **2022**, *75*, 310–320.

Manuscript received: January 10, 2023
Accepted manuscript online: March 20, 2023
Version of record online: April 25, 2023